Influence of the Preparation Method and Magnesium Ions Substitution on the Structure and Magnetic Properties of Lithium-Iron Ferrites

L. S. Kaykan and J. S. Mazurenko

1 Introduction

In recent years, ferrite-spinels of the general formula $(Me, Fe)_3O_4$, where M-divalent cation, attract considerable attention. This is due to not only to their excellent physical and chemical properties, but also to their technological applications, including magnetic storage devices, magnetic diagnostics, magnetic circuits, telecommunications, microwave devices, gas sensors, etc. [1–7] Each field of application requires from ferrites special properties, which can be reached by changing its synthesis conditions.

Ferrites have a high value of magnetization due to the imbalance of the magnetic moments of the lattice, a high value of resistance, low dielectric loss, and high Neel temperature [8–10]. These properties make ferrites universal materials for various technological applications. The crystallographic, electrical, and magnetic properties of ferrites are highly dependent on stoichiometry, as the parameters of the synthesis process, such as temperature, atmosphere, and pressure, affect the distribution of cations occupying tetrahedral (A) and octahedral (B) positions in the spinel lattice [11–14]. Control over the distribution of cations and oxygen parameters is important for the formation of physical properties that are necessary for the use of these materials in industry.

The morphology of the synthesized material, particle size, and their structure significantly affects their physicochemical properties. Thus, the preparation method is decisive even for ferrites of the same composition.

L. S. Kaykan (✉)
G.V. Kurdyumov Institute for Metal Physics, N.A.S. of Ukraine, 36 Academician Vernadsky Boulevard, Kyiv 03142, Ukraine

J. S. Mazurenko
Ivano Frankivsk National Medical University, Halytska Str. 2, Ivano-Frankivsk 76018, Ukraine
e-mail: yumazurenko@ifnmu.edu.ua

O. Fesenko and L. Yatsenko (eds.), *Nanomaterials and Nanocomposites, Nanostructure Surfaces, and Their Applications*, Springer Proceedings in Physics 263, https://doi.org/10.1007/978-3-030-74741-1_18

To establish the effect of the preparation method on the morphology and properties of magnesium-substituted ferrite with a spinel structure, the studied systems were synthesized in two ways. One system was obtained by the method of sol–gel auto combustion (system A) and the other by traditional ceramic method (system B). The structure and electrical properties of both systems are compared, and the influence of the method of preparation and substitution of magnesium ions on the physicochemical properties of the studied ferrites is revealed.

2 Experimental

Magnesium-substituted lithium ferrites of system A were synthesized by the sol–gel auto combustion method [15–17]. The production procedure was as follows: aqueous solutions of metal nitrates were used as starting reagents ($FeNO_3 \cdot 9H_2O$, $LiNO_3 \cdot 3H_2O$, $MgNO_3 \cdot 3H_2O$), taken in the appropriate molar ratio according to the stoichiometry of the expected compounds, as fuel used citric acid. Metal nitrates and citric acid were mixed dropwise on a magnetic stirrer in a molar ratio of metals to citric acid 1:1. The metal nitrate-citric acid solution slowly evaporated in the oven to form a viscous gel. Subsequent drying was performed to completely remove the adsorbed water at 110 °C. The resulting xerogel was placed in an oven, which was heated to a temperature of about 200–220 °C after which the mixture ignited and the exothermic reaction formed a product. Synthesized material was investigated using an X-ray diffractometer DRON-3 in CuK-α radiation. Figure 1 shows the precursor solution, the dried gel, and the product, formed after combustion.

Magnesium-substituted lithium ferrites of system B were synthesized by the ceramic method. Synthesis procedure included [18] the following mandatory steps:

1. Grinding of raw materials;
2. Preparation of the charging material;
3. Adding a plasticizer and forming a homogenized mixture;

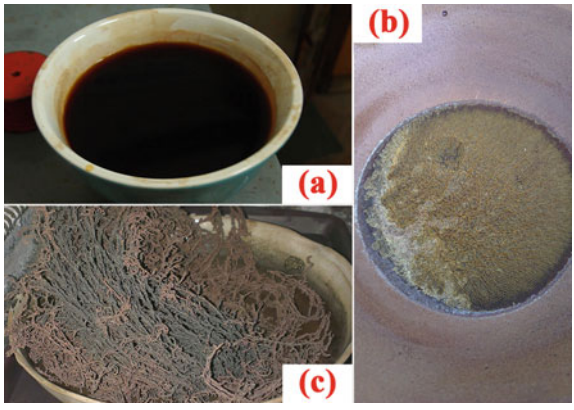

Fig. 1 Synthesis of lithium-iron spinel by sol–gel auto combustion method: **a** a solution of precursors; **b** dried xerogel; **c** the product, formed after the reaction

4. Formation of products;
5. Removal of the plasticizer;
6. Annealing of molded products.

To calculate the mixture of oxides (charging material) with the required ratio of components, we used the following procedure [19]: if the molar fraction of each of the components is a, b, c and the molecular weight is, respectively, a', b', c', the average molecular the weight of the mixture D is equal.

$D = aa' + bb' + cc'$. The weight percentages of the components of the mixture will be:

$$K_A = \frac{aa' \cdot 100}{D}; \quad K_B = \frac{bb' \cdot 100}{D}; \quad K_C = \frac{cc' \cdot 100}{D}$$

In our case, the composition of the charging material was calculated to obtain a spinel of general composition $Li_{0.5}Fe_{2.5-x}Mg_xO_4$, where $0.0 \leq x \leq 1.0$ with step 0.2. Starting oxides of Fe_2O_3 and MgO were of reagent grade (the content of the main component 98.8 and 98%) and LiOH—54.9%. The weight amounts of starting oxides to obtain 50 g of the substance are shown in Table 1.

The weighted portions of the starting oxides were thoroughly mixed and ground in a ball mill with the addition of distilled water for 2 h, after which the resulting mixture was evaporated, briquetted, air-dried at 120 °C, then pre-sintered in an oven at 900 °C for 5 h. The briquettes cooled together with the oven were carefully ground in a mortar to obtain a fine powder. Together with the plasticizer, the obtained powder was passed through a calibration grid with a cell size of 0.6 mm for homogenization. A 10% aqueous solution of polyvinyl alcohol is used as a plasticizer. As a result, we obtained a powder with an average particle size of ~0.1–0.2 μm. The obtained mass was used to form tablets 17 mm in diameter and 4 mm in height. To remove the plasticizer, the tablets were dried in air at a temperature of 120 °C for 8 h. The products obtained in this way were sintered in an oven at a temperature of 1000 °C for 5 h.

The obtained systems A and B were studied by X-ray structural, Mössbauer, and impedance methods.

Phase and structural analysis were performed using an X-ray diffractometer DRON-3 in CuK-α radiation. The full-profile Rietveld refinement method and the PowderCell program were used to analyze experimental diffractograms. Mössbauer absorption spectra of ^{57}Fe at room temperature were obtained in the mode of constant

Table 1 Amount of starting oxides, necessary to obtain spinel of general composition $Li_{0.5}Fe_{2.5-x}Mg_xO_4$

x	0.0	0.2	0.4	0.6	0.8	1.0
LiOH (g)	5.26471	5.34609	5.51663	5.79388	5.99472	6.20999
Fe_2O_3 (g)	48.78164	47.55424	44.98198	40.80041	37.77110	34.52423
MgO (g)	0.00000	1.00881	3.12297	6.55984	9.04965	11.71827

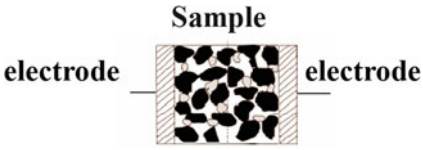

Fig. 2 Structure of the capacitor system for impedance spectroscopy

accelerations on a MS1104EM spectrometer using a source of γ-quanta ^{57}Co in a chromium matrix. Mathematical processing of the obtained spectra was performed using the universal computer program Univem [20].

To measure the spectrum of gamma-resonant absorption, which is the dependence of the intensity of resonant gamma radiation that has passed through the sample on the change in energy of resonant gamma quanta, the spectrometer used the principle of Doppler displacement of gamma quanta. To do this, the source is moved relative to the absorber, and at each value of the energy of gamma rays, which occurs during such a movement due to the Doppler effect, the intensity of gamma radiation passed through the sample is recorded.

Spinels of the composition $Li_{0.5}Fe_{2.5-x}Mg_xO_4$ ($x = 0.2$; 0.4; 0.6; 0.8) in powder form were used as an absorber. The density of the powder did not exceed 10 mg/cm^2.

Graphite electrode/sample/graphite electrode capacitor systems were fabricated for impedance studies (Fig. 2). Measurements were performed on an Autolab PGSTAT 12/FRA-2 impedance spectrometer in the frequency range 0.01 Hz–100 kHz.

3 Results and Discussion

3.1 Structure and Morphology of Magnesium-Substituted Lithium Ferrite

Figure 3 shows the experimental X-ray diffraction patterns of the system of magnesium-substituted lithium spinel, synthesized by the method of sol–gel auto combustion (system A) and by ceramic method (system B). As can be seen from the figure, all the obtained compounds are single-phase spinels; moreover, system with composition $Li_{0.5}Fe_{2.5}O_4$ ($x = 0.0$) belongs to the spatial group $P4_332$ [JCPDS No 76-1591], the so-called superordered spinel structure, as evidenced by the presence of superstructural peaks (110), (210), and (211). Such a superstructure arises due to the ordered arrangement of lithium and iron ions in a ratio of 1: 3 in the crystallographic direction [110]. All other compounds $Li_{0.5}Fe_{2.5-x}Mg_xO_4$, ($x = 0.2$; 0.4; 0.6; 0.8) found belonging to the spatial group Fd3m, because the presence of magnesium ions in the octa-lattice disrupts the order in the location of iron and lithium ions.

Figure 4 shows the experimental spectra of the samples of the composition

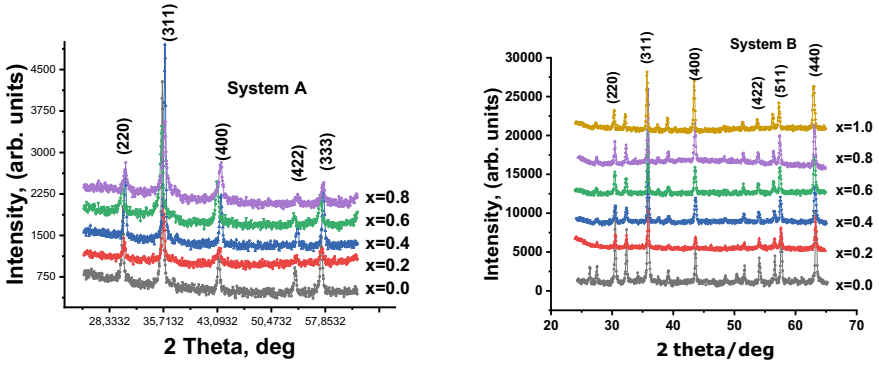

Fig. 3 Experimental X-ray diffraction patterns of systems $Li_{0.5}Fe_{2.5-x}Mg_xO_4$ ($x = 0.0; 0.2; 0.4; 0.6; 0.8$) obtained by sol–gel auto combustion method (system A) and experimental X-ray diffraction patterns of systems $Li_{0.5}Fe_{2.5-x}Mg_xO_4$ ($x = 0.2; 0.4; 0.6; 0.8; 1.0$), obtained by ceramic method (system B)

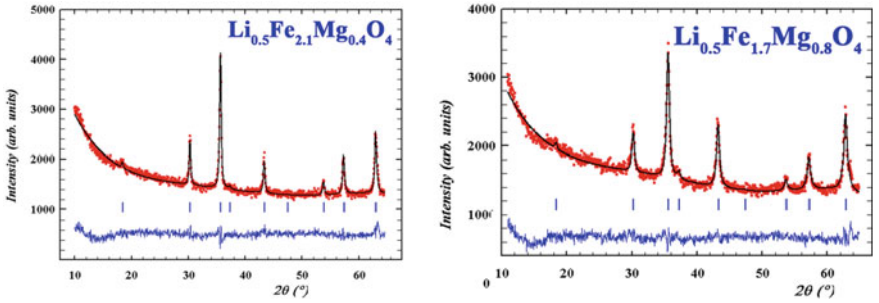

Fig. 4 X-ray spectra of compositions $Li_{0.5}Fe_{2.1}Mg_{0.4}O_4$ and $Li_{0.5}Fe_{1.7}Mg_{0.8}O_4$ (points) and their approximation by the full-scale Rietveld refinement method (solid line) (System B). Below is the difference spectrum

$Li_{0.5}Fe_{2.1}Mg_{0.4}O_4$ and $Li_{0.5}Fe_{1.7}Mg_{0.8}O_4$ (points) and their approximation by the full-profile Rietveld method (solid line). Below is the difference spectrum.

X-ray diffraction patterns of system B (samples obtained by ceramic method) for all Mg contents showed that the obtained system is identified as a single-phase defective cubic spinel structure from the spatial group Fd3m. Experimental X-ray diffraction patterns of samples in the vicinity of $20° \leq 2\Theta \leq 65°$ are presented in Fig. 3. The resulting system can be represented by the General formula $Li_{0.5}Fe_{2.5-x}Mg_xO_4$ ($x = 0.2; 0.4; 0.6; 0.8; 1.0$). Reflexes from the main reflecting planes (220); (311); (400); (511); (440); and (422) are observed in all diffractograms.

Figure 5 presents the experimental spectra of decoded using the FullProf software package.

The dependence of the constant lattice on the concentration with an accuracy of ± 0.002 Å, determined by X-ray diffraction for both systems is shown in Fig. 6.

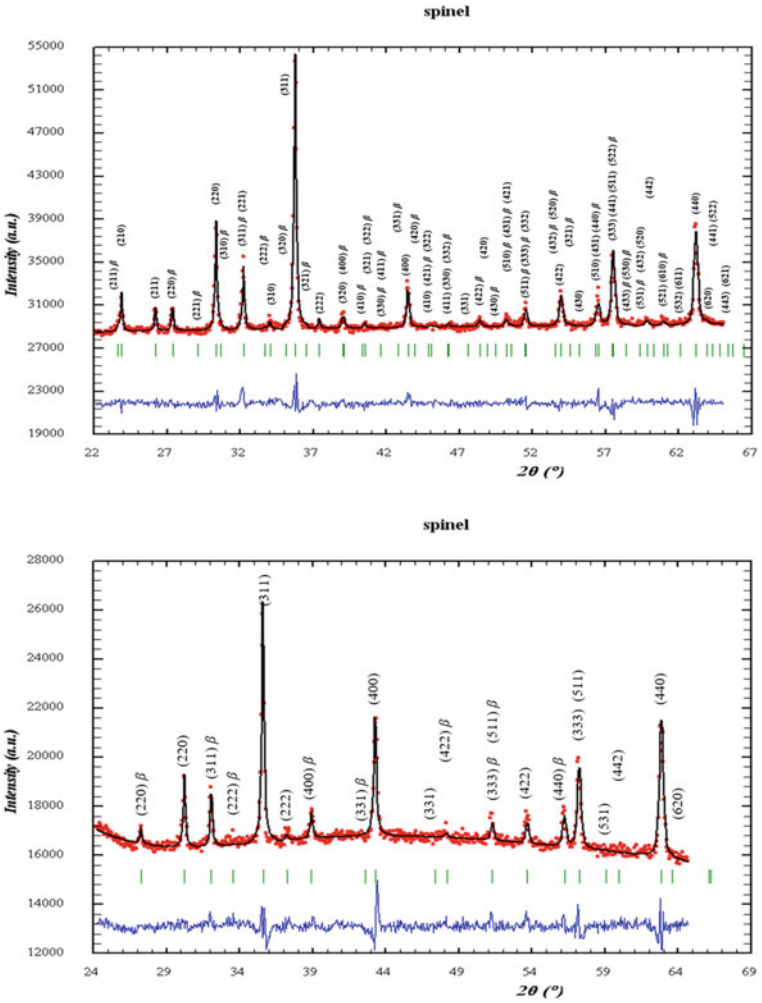

Fig. 5 Decoded X-ray diffraction patterns from a) the original (unsubstituted) sample $x = 0.0$ lithium-iron spinel b) from the sample of lithium-iron spinel, $x = 0.8$

The lattice constant value increases with increasing x for both systems. In the case of samples synthesized by the auto combustion method (system A), the values of the lattice constant are slightly higher than in system B. Obviously, this dependency of lattice constant behavior on the composition can be explained not so much by the substitution effect (because ions of approximately equal ionic radii Fe3 + (0.64) to Mg2 + (0.64) are replaced) but rather by the distortion of the unit cell caused by the formation of charged vacancies. Slightly larger values of the lattice constant for samples synthesized by ceramic method (system B) can be explained by the relatively

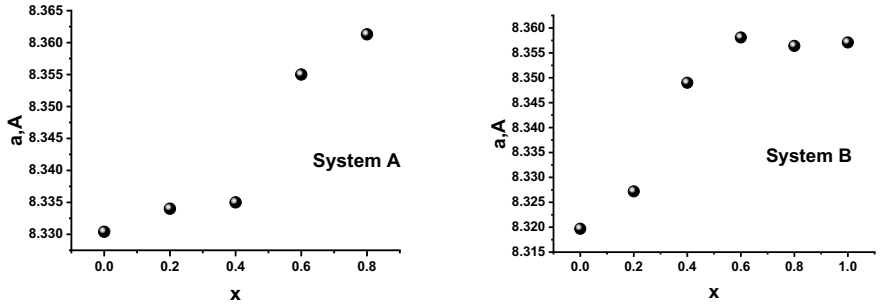

Fig. 6 Dependence of the lattice constant on the content of magnesium ions system A and system B

small size of the crystallites and, consequently, the influence of the surface. These results correlate well with the results obtained in [21].

For the system B, a small increase in the lattice constant a (Fig. 6) is associated with the formation of cationic and anionic vacancies, which occurs in nonstoichiometric substitutions and, according to [22], leads to an increase in the latter. And it should be noted the difference for both systems. For samples obtained by the ceramic method, the lattice undergoes changes at low levels of substitution, and in the case of auto combustion—at large. This difference is due to the fact that nonstoichiometric substitution in system B is accompanied by the formation of vacancies, which especially distort the lattice with small substitutions. With increasing magnesium content for such systems, the number of vacancies remains largely unchanged, as well as the magnitude of internal stresses increasing markedly with small substitutions, with increasing magnesium content remains almost the same. For samples obtained by auto combustion method (System A), the main reason for the increase in the lattice constant is the decrease in particle size observed during substitution.

The cationic distribution obtained from the analysis of experimental X-ray diffraction patterns using the full-profile Rietveld refinement method is shown in Table 2.

Table 2 shows that Li^+ cations occupy only the B position, while Fe^{2+} and Mg^{2+} ions occupy both A- and B-sublattice. Iron ions are redistributed on the A and B

Table 2 Distribution of cations by sublattices of systems $Li_{0.5}Fe_{2.5-x}Mg_xO_4$ ($x = 0.2$; 0.4; 0.6; 0.8) obtained by the method of sol–gel auto combustion

x	A-site	B-site	a (Å)	Δa (Å)
0.0	$Fe_{1.0}$	$Li_{0.5}Fe_{1.41}$	8.330	±0.002
0.2	$Mg_{0.16}Fe_{0.92}$	$Li_{0.5}Fe_{1.38}Mg_{0.04}$	8.334	±0.002
0.4	$Mg_{0.32}Fe_{0.84}$	$Li_{0.5}Fe_{1.26}Mg_{0.08}$	8.335	±0.002
0.6	$Mg_{0.48}Fe_{0.76}$	$Li_{0.5}Fe_{1.14}Mg_{0.12}$	8.355	±0.002
0.8	$Mg_{0.64}Fe_{0.68}$	$Li_{0.5}Fe_{1.02}Mg_{0.16}$	8.361	±0.002

Table 3 Distribution of elements by sublattices system B

x	Cationic distribution and phase composition	Spinel phase lattice parameters
0.0	$(Fe_{1.00})(Fe_{1.59}Li_{0.41})O_{4\pm\delta}$	8.3197 ± 0.0013
0.2	$(Li_{0.17}Fe_{0.76}Mg_{0.06})(Fe_{1.146}Li_{0.46}\ Mg_{0.08})O_{4\pm\delta}$	8.3272 ± 0.0013
0.4	$(Li_{0.16}Fe_{0.74}Mg_{0.09})(Fe_{1.57}Li_{0.33}\ Mg_{0.10})O_{4\pm\delta}$	8.3490 ± 0.0013
0.6	$(Li_{0.14}Fe_{0.66}Mg_{0.19})(Fe_{1.33}Li_{0.31}\ Mg_{0.36})O_{4\pm\delta}$	8.3581 ± 0.0013
0.8	$(Li_{0.19}Fe_{0.50}Mg_{0.31})(Fe_{0.94}Li_{0.41}\ Mg_{0.65})O_{4\pm\delta}$	8.3564 ± 0.0013
1.0	$(Li_{0.22}Fe_{0.35}Mg_{0.44})(Fe_{0.68}Li_{0.44}\ Mg_{0.88})O_{4\pm\delta}$	8.3571 ± 0.0013

sublattices in a ratio of approximately 4:6 and magnesium ions 8:2, respectively. According to the results of X-ray diffractometry, the advantages of the B position of the above ions are as follows: $Li^+ > Fe^{3+}Mg^{2+}$.

For samples of system B, the calculation of the cation distribution was carried out taking into account the ionic radii of each position (r_A and r_B) for different compositions. The results of calculations for all systems are presented in Table 3. In the unsubstituted lithium-iron spinel of stoichiometric composition $Li_{0.5}Fe_{2.5}O_4$, obtained under equilibrium synthesis conditions, all lithium atoms are localized in the octa-lattice, while iron ions are placed in tetra- and octa-positions (the case of the inverted spinel). Since one subsystem contains elements whose valence differs by 2 (in our case Li^+ and Fe^{3+}) at a low rate of synthetic cooling, the formation of a superstructure is possible [23], i.e., the process of atomic 1:3 ordering in the octa-sublattice, resulting in three Fe^{3+} ions and one Li^+ ion all are naturally located along the crystallographic directions <110> . In other words, as a result of a phase transition of the ordering type, a spatial group $O_h^7 - Fd3m$ decreases to $O^7 - P4, 3$. The diffraction pattern of the slowly cooled stoichiometric unsubstituted sample revealed the corresponding superstructural reflexes (110), (210), (211) (Fig. 6), which are absent on the diffractograms of the other samples: nonstoichiometric doping leads to the destruction of the superordination in the octa-sublattice.

Sintering of spinel at high temperatures and its subsequent cooling is accompanied by the following processes: redistribution of ions between the sublattices; ordering of ions within individual lattices, annihilation or association of point defects with cluster formation, spinel phase decay, as well as loss of volatile cations (Li^+) and oxygen [24]. Oxygen leaving the lattice at high temperatures comes from the atmosphere during cooling and is introduced into the structure, restoring the anionic sublattice. This oxygen can occupy both regular and irregular positions, causing minor tetragonal distortions [25]. Lack and excess of oxygen, as well as its presence in irregular positions causes significant changes in the structure and electrical properties of the studied materials.

Table 3 shows the distribution of system components by tetrahedral and octahedral positions of the spinel. A gradual decrease in the iron content in both sublattices and a simultaneous increase in magnesium indicates an almost uniform entry of Mg^{2+} ions in both sublattices in a ratio close to 1:2. Lithium ions are also redistributed in both sublattices almost evenly.

In general, according to system B, the substitution of Fe^{3+} ions for Mg^{2+} ions leads to a violation of electroneutrality, which increases with increasing magnesium content. In these systems, it is unlikely to provide a charge balance by increasing the valence of iron to the state of Fe^{4+}. Therefore, we can assume that electroneutrality is provided mainly by lithium vacancies and the introduction of cations in irregular positions, which, according to [26] leads to the formation of F-centers (the presence of a charged ion in the irregular position or the absence of the latter in the regular), strongly affects the processes of charge transfer in such systems.

The values of the sizes of the coherent scattering regions (CSR) for the samples of system A were calculated by the Selyakov-Scherrer formula.

$$\langle D \rangle = \frac{\lambda}{\beta_{\frac{1}{2}} \cos\theta},$$

where λ—X-ray wavelength, θ-diffraction angle, and $\beta_{1/2}$—half-width of reflection. Also, by the Williamson-Hall interpolation method, according to which the dependence of $\beta\cos\theta$ on the $\sin\theta$ equation

$$\beta \cos\theta = \frac{\lambda}{D} + 4\varepsilon \sin\theta$$

was constructed (if the approximation was performed by Lorentz or Cauchy functions) or equation

$$\beta^2 \cos^2\theta = \left(\frac{\lambda}{D}\right)^2 + (4\varepsilon \sin\theta)^2$$

(if the approximation was carried out by the Gaussian function). If we linearly approximate the obtained dependence, the angle of inclination of the line will be proportional to the magnitude of microstrains (ε or ε^2), and the intersection of the line with the y-axis is a quantity inversely proportional to the size of the CSR (D or D^2).

Figure 7 shows the Williamson-Hall dependence for the sample of $Li_{0.5}Fe_{2.5}O_4$ composition, and Table 4—calculated the CSR values for all synthesized systems by both the Scherrer method and the Williamson-Hall method.

The data in Table 4 indicate that all the synthesized samples are nanoscale, and larger values of the experimental constant lattice compared to the theoretical caused by the influence of the surface due to the small size of the crystallites. Slightly larger values of CSR in the Selyakov-Scherrer method are due to the fact that only one peak of intensity (the third) was taken into account, and the Williamson-Hall method takes into account all reflexes. It is known that with increasing the angle of reflection, the half-width of the peak increases, so taking into account, all the reflexes can give an average value, which may be slightly less than for one randomly selected reflex. Also, when determining the value of $\beta_{1/2}$ was taken into account the

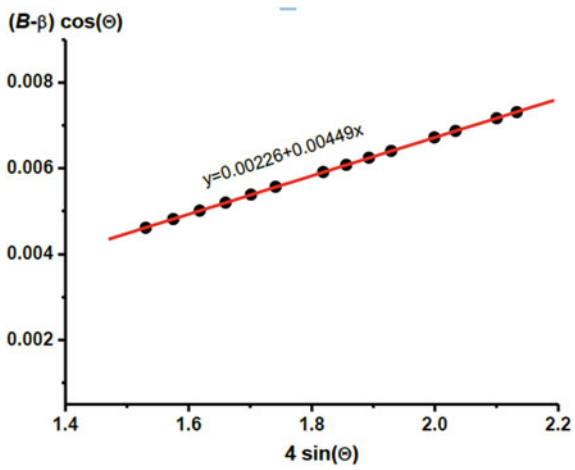

Fig. 7 Williamson-Hall dependence for the system $Li_{0.5}Fe_{2.5}O_4$

Table 4 Size of the coherent scattering (CSR) regions of the systems $Li_{0.5}Fe_{2.5-i}Mg_xO_4$ ($x = 0.0$; 0.2; 0.4; 0.6; 0.8) obtained by the method of sol–gel auto combustion, determined by the methods of Selyakov-Scherrer and Williamson-Hall

Concentration, x	CSR (nm) Selyakov-Scherrer method	CSR (nm) Williamson-Hall method
0.0	42.0	40.0
0.2	17.0	16.8
0.4	24.0	23.6
0.6	16.0	15.4
0.8	15.0	14.4

instrumental broadening caused by the discrepancy of the X-ray beam and the width of the limiting slits, which was determined using a reference sample. This sample was a well-annealed sample of lithium-iron spinel obtained by ceramic method.

3.2 Mössbauer Studies of Mg-Substituted Lithium-Iron Spinels

The spectrum of the unsubstituted sample ($x = 0.0$) consists only of magnetically ordered components. Of these, sextets with a magnetic field value of 507.78 and 496.87kOe can be attributed to iron ions in the octahedral and tetrahedral lattices, and a sextet with H = 455.53kOe can obviously be attributed to iron ions in the surface state, i.e., at the grain boundaries (Fig. 8).

With substitution on the spectra, a paramagnetic doublet appears, the intensity of which increases with increasing magnesium content.

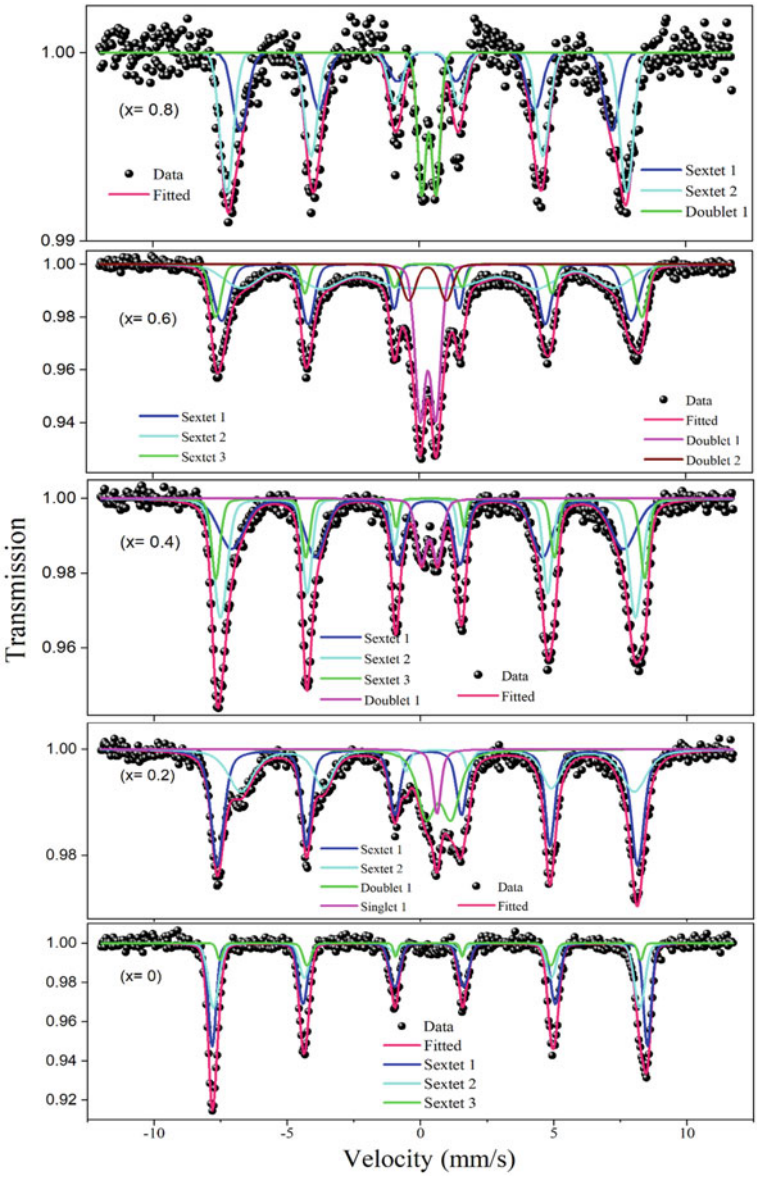

Fig. 8 Presents the Mössbauer spectra of 57Fe at room temperature of the system A $Li_{0.5}Fe_{2.5-x}Mg_xO_4$ ($x = 0.0; 0.2; 0.4; 0.6; 0.8$).

The parameters for decoding the Mössbauer spectra of all synthesized systems are given in Table 5.

Mössbauer spectra from ^{57}Fe, system B, obtained at room temperature for all samples, revealed an asymmetric Zeeman magnetic picture (Fig. 9). This magnetic sextet coexists with two paramagnetic doublets. The asymmetry of magnetically ordered components assumes the presence of two different superfine magnetic sextets, one of which can be attributed to the tetrahedral and the other to the octahedral environment of oxygen in the spinel lattice. However, when the content of magnesium ions in the structure increases, a central quadrupole doublet is observed along with the broadening of the magnetic sextet.

The intensity of this doublet increases with increasing concentration of Mg^{2+} ions, which for all systems coexists with the magnetically ordered phase, which remains pronounced at high concentrations of embedded magnesium. The observed general broadening of the Mössbauer lines for A- and B-sextets can be caused by a change in the chemical environment around different iron ions in the same sublattice. The value of the isomeric shift corresponding to the coordination of Fe^{3+} did not change significantly with increasing concentration of Mg^{2+} ions at room temperature. This fact indicates that the charge of s-electrons, which is distributed on Fe^{3+} ions, is almost independent of the content of substituted Mg^{2+} ions. The isomeric shift of the octahedral positions was found to be slightly less positive than for the tetrahedral ones (Table 6), which may be due to the slight sp3 covalence that occurs for ions at the B positions.

The parameters of the Mössbauer spectra of system B, calculated using the computer program MossWin (Table 6), give the characteristics of Fe^{3+} ions occupying tetrahedral (A) and octahedral (B) positions of the spinel structure.

The widths of the lines corresponding to the tetrahedral and octahedral environment of Fe^{3+} increase with increasing content of Mg^{2+} ions (Table 6), and accordingly, the superfine magnetic fields decrease (Fig. 9), which indicates the entry of magnesium ions into both octa- and tetrahedral positions.

Table 7 compares the data on the cationic distribution of iron obtained from Mössbauer and X-ray experiments.

The distribution of iron ions on the sublattice for X-ray data is taken from the proposed cationic distribution and expressed as a percentage relative to the total iron content in the sample. For Mössbauer data, the content of this distribution was calculated from the total area of sextets responsible for the tetra and octa, and the intensity of paramagnetic doublets was taken into account.

As can be seen from Table 7, the distribution of iron on octa- and tetra-sublattices calculated from Mössbauer data taking into account the intensity of paramagnetic doublets and X-ray diffraction patterns (Tables 5 and 6) generally coincides, which indicates the correctness of the results. Slight differences in the ratios can obviously be explained by the limitations of each of the methods and the disregard for the probability of the Mössbauer exit from different sublattices.

Mg^{2+} ions are known to have a weak advantage in the octahedral positions, as do Li^{+} ions, which also tend to occupy octahedral positions. According to Neel's molecular field theory [27], in spinels, the A-B-super-exchange interaction dominates the

Table 5 Parameters for decoding Mössbauer spectra of system A

Sample	$Li_{0.5}Fe_{2.5}O_4$	$Li_{0.5}Fe_{2.3}Mg_{0.2}O_4$	$Li_{0.5}Fe_{2.1}Mg_{0.4}O_4$	$Li_{0.5}Fe_{1.9}Mg_{0.6}O_4$	$Li_{0.5}Fe_{1.7}Mg_{0.8}O_4$
Is	0.3557	0.2761	0.2862	0.2330	0.2620
Qs	0.0080	−0.0271	0.0076	0.0592	−0.0336
H_{eff}	507.76	489.64	466.87	442.01	433.07
S	40.29	47.95	45.30	24.42	32.30
G	0.3500	0.5657	0.6631	0.7721	0.6697
Is	0.2606	0.6365	0.3102	0.3014	0.2801
Qs	−0.0169	0.0008	0.011	−0.0063	−0.0091
H_{eff}	496.87	458.42	494.40	490.24	465.98
S	51.04	29.83	44.87	40.17	51.34
G	0.4525	1.1230	0.4450	0.3677	0.5898
Is	0.3356				
Qs	−0.504				
H_{eff}	455.53				
S	8.67				
G	0.7760				
Is		0.6788	0.3512	0.3107	0.3555
Qs		0.9258	0.6723	0.6526	0.5293
S		18.14	9.82	35.40	16.36
G		0.8030	0.5205	0.6915	0.3896
Is		0.6141			
S		4.08			
G		0.3600			

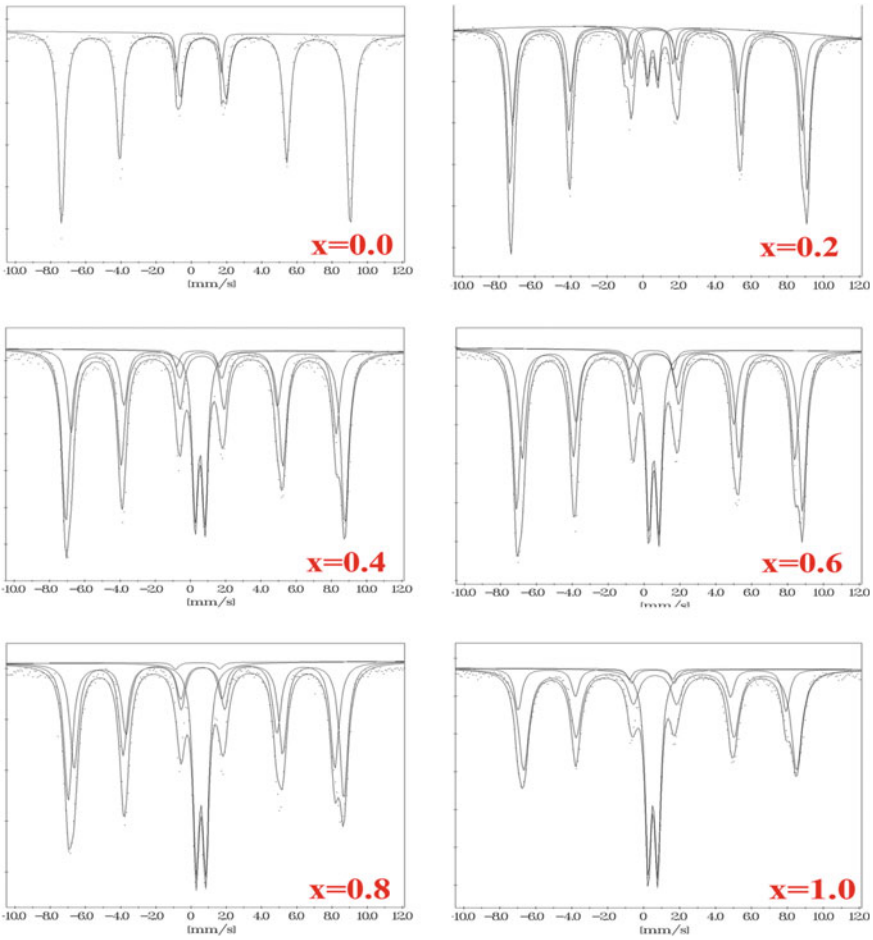

Fig. 9 Experimental ^{57}Fe Mössbauer spectra of synthesized systems B, measured at room temperature

intra-sublattice A-A and B-B interactions, and the internal superfine magnetic fields of the octa- and tetra-environment decrease with increasing Mg^{2+} substitution. In the unsubstituted sample, all lithium ions are concentrated in the octa-sublattice, and when substituted with magnesium, the latter displaces lithium in the tetra-sublattice. However, due to the weak advantage to the octa-positions, magnesium enters both sublattices, reducing the magnetic fields on the nuclei in both subsystems.

A paramagnetic doublet with a quadrupole close to 2.5 can be considered a sign of the presence of divalent iron, the concentration of which in the octahedral subsystem is quite small. The presence of Fe^{2+} in the tetra-sublattice is unlikely, due to its large ionic radius (0.83 nm). The second paramagnetic doublet, the intensity of which increases with increasing Mg^{2+} ion content, can be attributed to the manifestation of

Table 6 Parameters for decoding Mössbauer spectra of system B

Sample	$Li_{0.5}Fe_{2.5}O_4$	$Li_{0.5}Fe_{2.3}Mg_{0.2}O_4$	$Li_{0.5}Fe_{2.1}Mg_{0.4}O_4$	$Li_{0.5}Fe_{1.9}Mg_{0.6}O_4$	$Li_{0.5}Fe_{1.7}Mg_{0.8}O_4$
Is	0.755	0.7	0.67	0.70	0.68, 0.49
Qs	0.15	0.18	0.17	0.20	0.18, −0.05
H_{eff}	50.89	49.66	46.66	47.13	45.92, 46.27
S	95.40	33.65	24.76	32.49	34.05, 15.59
G	0.46	0.41	0.50	0.51	0.58, 0.49
Is		0.77	0.75	0.76	0.76, 0.77
Qs		0.19	0.19	0.19	0.17, 0.28
H_{eff}		51.07	49.15	49.43	48.55, 47.13
S		54.85	54.52	46.01	42.75, 54.24
G		0.41	0.53	0.50	0.56, 0.71
Is					
Qs					
H_{eff}					
S					
G					
Is		0.54	0.55	0.54	0.56, 0.51
Qs	–	0.56	0.56	0.57	0.55, 0.54
S		6.62	18.72	19.21	22.40, 28.58
G		0.30	0.39	0.39	0.42, 0.40
Is	0.45	0.33	0.43	0.40	0.38, 0.41
Qs	2.54	2.68	2.43	2.44	2.51, 2.41
S	4.61	4.88	1.99	2.29	0.80, 1.59
G	0.21	0.30	0.39	0.39	0.42, 0.40

Table 7 Cationic distribution of iron obtained from Mössbauer and X-ray experiments

X	X-ray analysis			Mössbauer analysis		
	Fe_{okt} (%)	Fe_{tetr} (%)	Fe_{okt} / Fe_{tetr}	Fe_{okt} (%)	Fe_{tetr} (%)	Fe_{okt} / Fe_{tetr}
0.2	60.0	37.5	1.6	61.9	38.1	1.6
0.4	65.9	34.1	1.9	65.9	34.1	1.9
0.6	66.0	34.0	1.9	67.5	32.5	2.0
0.8	66.1	33.9	1.9	65.9	34.1	1.9
1.0	69.4	30.6	2.3	70.1	29.9	2.3
Error	±0.1	±0.1	±0.1	±0.1	±0.1	±0.1

superparamagnetism, which is typical for the replacement of ferrites by nonmagnetic ions, for example, in Li–Zn ferrites [28], $CoFe_{2-x}Al_xO_4$ [29], and a number of others.

The presence of a central quadrupole doublet together with a widened magnetic sextet was observed in [28–30], and it was given various explanations. The possibility of a central doublet as a consequence of the presence of a paramagnetic impurity is incomplete, as the results of X-ray diffraction indicated the presence of only one pure spinel phase. Some samples were re-fabricated, but they did not show any changes in the presence of the center line. Moreover, it was found (Table 6) that the intensity of the doublet increases with increasing concentration of Mg^{2+} ions. It is known [29] that with increasing number of diamagnetic ions, some Fe^{3+} ions are isolated from other magnetic ions and have a short-term magnetic order. This promotes the growth of magnetic clusters of different sizes, known as superparamagnetic clusters, which have very little magnetic interaction with the environment, but which can have any type of magnetic arrangement within the cluster. Small clusters are characterized by a faster degree of relaxation, which causes the growth of the paramagnetic doublet. In such systems, magnetically ordered clusters are separated from others by nonmagnetic ions. A similar picture of the coexistence of magnetically ordered systems and a paramagnetic cluster (with a small quadrupole) was observed in [10] and explained on the basis of two relaxation mechanisms: spin–spin relaxation and relaxation between the possible direction of the spin slope in relation to "spin glass." In [31], the growth of the central doublet based on the Zeeman magnetic pattern in ferrites with diamagnetic substitution is explained by the formation and development of clusters with a decrease in magnetic A–B bonds. It was noted that when discrete subspectra, including the central component, were used to approximate the picture, Fe^{3+} ions did not have an advantage to any particular position.

A similar phenomenon of superimposition on the magnetic picture of the central paramagnetic line was observed in the study of the $ZnCr_xGa_{2-x}O_4$, $0.2 \leq x \leq 2$ system in [27]. However, in this case, the phenomenon is related to the existence of a dependence similar to spin glass, and the results are explained using the concept of two spin clusters. In other works, such as [10, 30], the presence of a central doublet was explained on the basis of the assumption of the presence of entropic clusters rather than superparamagnetic.

As the content of nonmagnetic Mg^{2+} ions increases both in the octa- and in the tetra-sublattices, there is a "break" of super-exchange bonds of type AB between the two sublattices, and as a consequence, there is an increase in the intensity of the quadrupole doublet with decreasing magnetic fields on the nuclei also in both subsystems, as observed in this work.

3.3 Frequency Behavior of Conductive and Dielectric Properties of Mg-Substituted $Li_{0.5}Fe_{2.5}O_4$ Spinels

Impedance spectroscopy is an effective method for studying the reproducibility of a cathode substance and the peculiarities of charge transfer processes in it. Experimental studies of complex impedance were used to study the properties of solid electrolytes [22] and ceramic oxides [23], and data analysis is based on the possibility of model representation of the test substance by an equivalent scheme. The determined parameters of such a scheme are compared with the corresponding values that characterize the conductive and dielectric properties of the components of the studied systems.

In this work, the influence of the conditions of synthesis and nonstoichiometric substitution of iron in the $Li_{0.5}Fe_{2.5}O_4$ matrix by divalent magnesium ions on the frequency behavior of the conductive and dielectric properties of the material was investigated by impedance spectroscopy methods.

System B is characterized by the presence of an ionic component of conductivity, as evidenced by hodographs (Fig. 10) in the form of a semicircle and a pronounced polarization branch, which goes to infinity with decreasing frequency [21] (Fig. 11).

The equivalent circuit (Fig. 12) is a series-connected two RC-elements, the resistance, and capacitance of which characterize the grain and intergranular regions and the area of the circle containing the Warburg element. The value of the Warburg element W is due to the diffusion transfer of lithium in the structure:

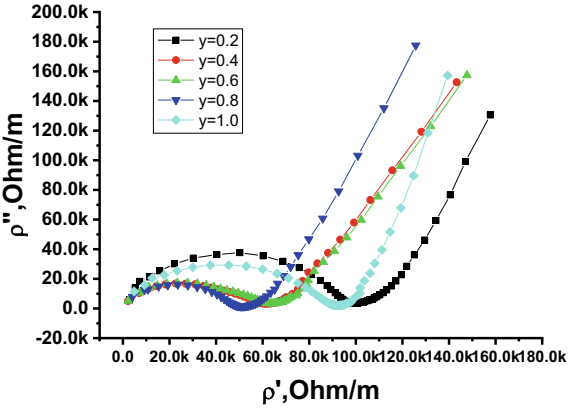

Fig. 10 Nyquist diagrams for specific values of real and imaginary part of resistance od system B

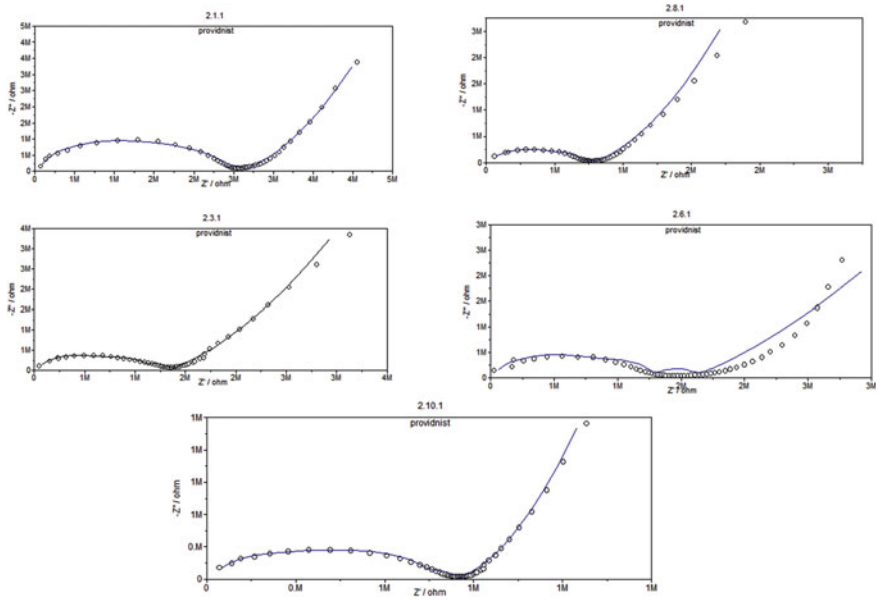

Fig. 11 Experimental (points) and frequency dependences calculated according to equivalent schemes (solid lines) of real and imaginary part of resistance

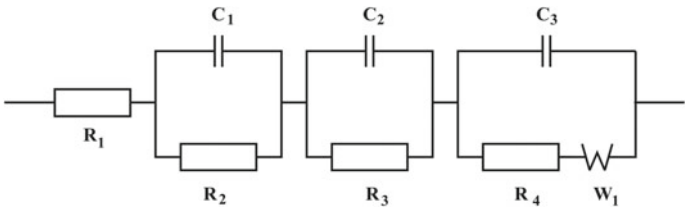

Fig. 12 Equivalent circuit

$$W = \frac{RT}{n^2 F^2 c_{Li} \sqrt{2D}}$$

where c_{Li}—volume concentration of lithium at a given electrode potential; D—diffusion coefficient; F—Faraday constant; T—absolute temperature.

However, in the nonstoichiometric system $Li_{0.5}Fe_{2.5-x}Mg_xO_4$, the degree of substitution of iron by magnesium determines different contributions to the specific conductivity of the ionic and electronic components, and the hodograph curves cannot be modeled in semicircles even for deposits with low values x. Therefore, the simulation should be performed taking into account the deformation of the circuits along the axis, which is expressed in the replacement of the capacitor by a constant phase

Table 8 Parameters of model representation of impedance measurements of magnesium-substituted lithium-iron spinels, which were slowly cooled by the synthesis temperature

x	R_1 (kΩ)	R_2 (kΩ)	R_3 (kΩ)	C_1 (pF)	C_2 (μF)	W
0.1	70.1	768.1	208.4	77.5	8.6	0.2
0.3	46.1	442.2	225.1	125.3	9.6	0.2
0.6	34.6	484.5	294.1	113.9	1.8	0.2
0.8	43.5	235.1	85.6	123.6	9.8	0.3
1.0	21.7	327.4	79.4	85.3	19.1	0.8
Error	±0.1	±0.1	±0.1	±0.1	±0.1	±0.1

element [31], the physical meaning of which is that the frequency impedance dispersion becomes similar to an inhomogeneous transmission line. Thus, the simulation of impedance hodographs should be performed taking into account both the multi-stage RC-system and the mass–charge transfer system. Table 8 shows the calculated values of the components, expressed by the electrical elements of the sections of equivalent circuits for sample of system B. In Table 8, the resistance R_1 corresponds to the resistance of the electrodes and contacts, and the resistances R_2 and R_3—the resistance of the crystallites and intercrystalline gaps. Since these systems are single-phase, the impedance hodograph is satisfactorily modeled by two sections, one of which expresses the electrophysical properties of the crystallites, and the other—the intercrystalline gaps. This partition, carried out on the basis of Wagner-Koops theory [32], is valid, as these structural components are characterized by strong differences in the values of the calculated parameters. The need to introduce the Warburg diffusion coefficient into an equivalent scheme was determined by the presence of a clearly expressed polarization branch in the Nyquist experimental diagrams, which indicates the presence of diffusion processes (Figs. 10 and 11).

In the study of electrical conductivity [33, 34], it is suggested that the electrons involved in the formation of electric current are localized mainly in the locations of

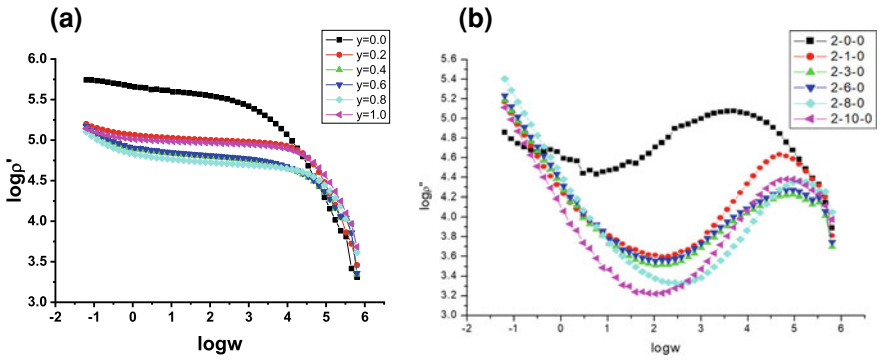

Fig. 13 Dependence of the real part (**a**) and imaginary part (**b**) of the resistivity on the frequency (system B)

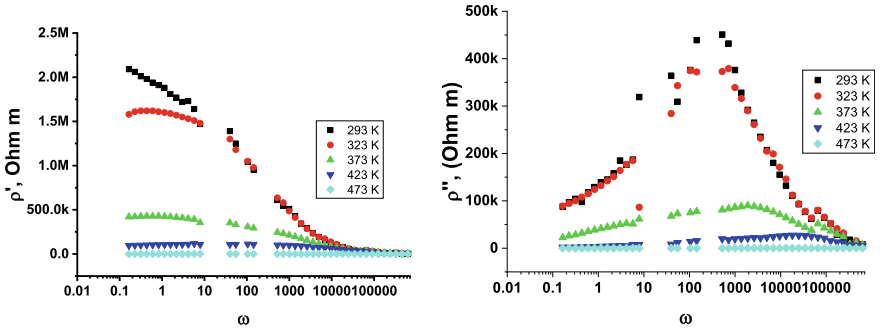

Fig. 14 Frequency dependence of real and imaginary parts of resistivity at different temperatures system A

ions. Based on the assumption of the localization of the states of 3d-electrons, we can imagine the process of electric current as a process of jumping electrons from one ion to another. Thus, it is considered that the corresponding valence states of the ions themselves migrate along the crystal, and at a sufficiently high concentration of ions with variable valence, the electrical conductivity is of high value and is characterized by low activation energy. In the presence of variable valence ions in the structure, in our case ions of ferrous and trivalent iron, 3d—the electron of the Fe^{2+} ion, overcoming the energy barrier, can jump to the Fe^{3+} ion, resulting in a process:

$$Fe^{2+} + Fe^{3+} \leftrightarrow Fe^{3+} + Fe^{2+}.$$

This process can occur in the absence of an external electric field. In this case, the system is in a state of dynamic equilibrium, in which the charge transfer is chaotic without a selected direction, so that the total current through an arbitrary cross section is zero. The situation changes in the case of applying an external electric field. The statistical distribution of electron jumps changes, their relative frequency increases in a certain direction, and there is a directed drift of electrons, so that the resulting current becomes different from zero.

Based on the hopping mechanism, the electrical conductivity of these systems largely depends on the content of divalent ions. The value of conductivity is directly dependent on the concentration of Fe^{2+} ions in the compound, which, in turn, depends on the composition of the initial oxides and the synthesis conditions. As can be seen from the results of Mössbauer analysis, almost every sample of system 2 includes iron in the divalent state. As shown by the results of the frequency dependence of conductivity, in the case of system B, the conductivity is greater than in system A. Thus, the amount of iron in the divalent state is responsible for the value of conductivity in the system.

Frequency dependences of the loss tangent (tan(δ)), for spinels of the composition $Li_{0.5}Fe_{2.5-x}Mg_xO_4$, where $x = 0.0; 0.1; 0.3; 0.6; 0.8; 1.0$ measured for the frequency

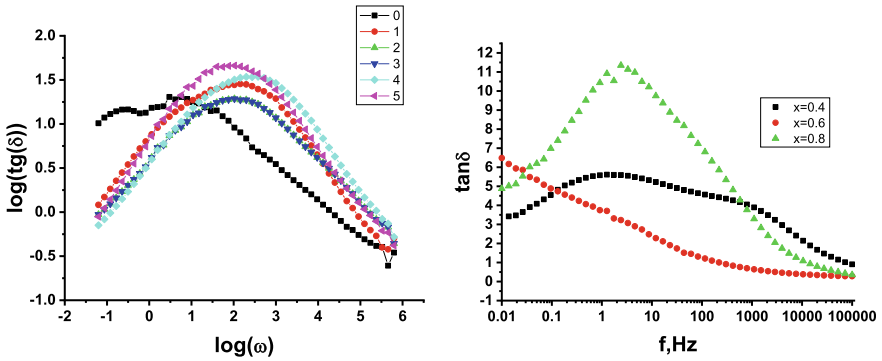

Fig. 15 Frequency dependences of the loss tangent (tan(δ)) of system B; dependence of the dielectric loss tangent (tan(δ)) on frequency of $Li_{0.5}Fe_{2.1}Mg_{0.4}O_4$, $Li_{0.5}Fe_{1.9}Mg_{0.6}O_4$, and $Li_{0.5}Fe_{1.7}Mg_{0.8}$, synthesized by the method of sol–gel auto combustion

range from 10^{-2} to 10^5 Hz. The change in tan(δ) with frequency at room temperature is shown in Fig. 15.

The figure shows that the dependence of the loss tangent on the frequency for systems $Li_{0.5}Fe_{2.1}Mg_{0.4}O_4$ and $Li_{0.5}Fe_{1.7}Mg_{0.8}$ characterized by the presence of a peak (for the system $Li_{0.5}Fe_{2.1}Mg_{0.4}O_4$ two of them, with vertices in the frequency range of 10 and 1000 Hz), indicating the resonant nature of the polarization processes in these systems. The maximum in tan$\delta(f)$ can be observed when the jump frequency is approximately equal to the frequency of the external applied field. The conditions for observing the maximum in tan$\delta(f)$ are given by the relation [35]:

$$\omega'\tau \approx 1$$

where $\omega' = 2\pi f_{\max}$ and $f_{\max}$ is proportional to the probability of a jump, τ—relaxation time.

Another explanation for the occurrence of the peak in the change of the tangent of losses with frequency can be made taking into account the dispersion of the dielectric constant. The presence of such a maximum can be explained by the fact that the rate of decrease of the real part of the dielectric constant in the frequency range $f < f_{\max}$ increases and at $f > f_{\max}$ decreases, as shown in Fig. 15, which may cause a peak in tan(δ) versus frequency. The double peak in the frequency dependence of the loss tangent for the system is obviously associated with both the processes of electron jump and the polarization of grain boundaries, which in fine materials make a significant contribution to both conduction and polarization processes due to the accumulation of defects and various kinds of inhomogeneities.

4 Conclusions

It is found that all magnesium-substituted systems are single-phase spinels of the spatial group Fd3m; the unsubstituted sample of the composition $Li_{0.5}Fe_{2.5}O_4$ ($x = 0.0$) belongs to the spatial group $P4_332$ [JCPDS No 76-1591], the so-called super-ordered spinel structure. The obtained systems belong to the nanometer range with CSR sizes of ~20–40 nm. As the concentration of magnesium (x) increases, the tetrahedral radii gradually increase, while the octahedral ones decrease. Total ionic radius $\overline{r}$ ($\overline{r} = \frac{r_A + r_B}{2}$) increases more slowly, which is reflected in the increase of the lattice constant. Thus, it is possible to note that substitution in a tetrahedral position plays a dominant role depending on change of a constant lattice on structure. It is shown that Li^+ cations occupy only B positions, while Fe^{3+} and Mg^{2+} ions occupy both A- and B-lattice. Iron ions are redistributed on the A and B sublattices in a ratio of approximately 4:6 and magnesium ions 8:2, respectively. According to the results of X-ray diffractometry, the advantages of the B position of the above ions are as follows: $Li^+ > Fe^{3+} > Mg^{2+}$.

X-ray density decreases with increasing x. This is due to the fact that the atomic weight of Mg^{2+} (24.31) is less than that of Fe^{3+} (55.8). Calculation of bond lengths between cations (b, c, d, e, f) (Me-Me) and between cation and anion (p, q, r, s) (Me-O), calculated on the basis of experimental values of the constant lattice and oxygen parameter (u), showed that both parameters increase with substitution, which leads to a weakening of the magnetic interaction in the system.

Studies of the conductive and dielectric properties of magnesium-substituted lithium-iron spinels based on impedance spectroscopy have shown: (1) the studied systems are characterized by the presence of two conduction mechanisms: electronic and ionic; (2) electronic conductivity is based on the jumping mechanism due to the presence of ferrous ions and is realized mainly by the volume of grains in the octa-lattice of spinel; (3) diffusion transfer of lithium ions is carried out at intergranular boundaries and point defects (vacancies), the number of which increases as the system deviates from stoichiometry; (4) with increasing number of ions of embedded magnesium system B, the value of conductivity at direct current does not change due to participation in the jumping mechanism of stable complexes $\left[Li^+_{tetra}Fe^{3+}_{octa}\right]$, formed during substitution; (5) the sharp increase in conductivity for system B is determined by the high content of ferrous ions, which is due to the use of high temperatures and long heat treatment times during synthesis; (6) the samples of system A are characterized by a decrease in conductivity with an increase in the content of embedded magnesium ions, which is due to a decrease in the number of Fe^{2+} ions; (7) the samples of system A and system B are characterized by different nature of the decrease in the real part of the dielectric constant, which is obviously due to differences in the microstructure. Moreover, the samples of system A show a significant dependence of the loss tangent on the composition; (8) polarization processes for system B are characterized by a constant relaxation time, and for system A, the relaxation time depends on the composition, which, obviously, is also determined by differences in the microstructure.

Thus, the study of the influence of synthesis conditions on the properties of magnesium-substituted lithium ferrites showed that in the case of synthesis by sol–gel auto combustion, there is a decrease in the size of synthesized particles by almost 10 times, which indicates high dispersion of Li-Mg ferrite system and increased 20 times the specific surface area of the substance.

Sol–gel synthesis results in nano disperse particles with higher porosity, higher lattice value, and degree of lithium stoichiometry, while remaining single-phase systems as in ceramic synthesis, but the samples obtained by sol–gel method have a more perfect structure and are high stoichiometry.

The obtained results showed the expediency of using the sol–gel method of auto combustion for the synthesis of high-quality nanosized ferrites with improved technological characteristics.

References

1. Akhtar MN, Yousaf M, Lu Y, Khan MA, Sarosh A, Arshad M, Niamat M, Farhan M, Ahmad A, Khallidoon MU (2021) Ceramics International
2. Fantechi E, Innocenti C, Bertoni G, Sangregorio C, Pineider F (2020) Nano Res 13:785
3. Thota S, Singh S (2017) Magnetic spinels—synthesis, properties and applications. InTech
4. Zhang Y, Yuan L, Zhang X, Zhang J, Yue Z, Li L (2017) Appl Surf Sci 410:99
5. Uhorchuk OM, Uhorchuk VV, Karpets MV (2015) J Nano-Electron Phys 7(2)
6. Deepty M, Srinivas Ch PN, Ramesh N, Mohan K, Singh MS, Prajapat CL, Verma A, Sastry DL (2020) Sens Actuators B Chem 316:128127
7. Hao X, Liu T, Li W, Zhang Y, Ouyang J, Liang X, Liu F, Yan X, Zhang C, Gao Y, Wang L, Lu G (2020) Sens Actuators B Chem 302:127206
8. Ostafijchuk BK, Bushkova VS, Moklyak VV, lnitsky RV (2015) Ukr J Phys 60:1234
9. Soman VV, Nanoti VM, Kulkarni DK (2013) Ceram Int 39:5713
10. Kotsyubynsky V, Moklyak V, Hrubiak A (2014) Mater Sci-Pol 32:481
11. Kopayev AV, Mokljak VV, Gasyuk IM, Kozub VV (2015) SSP 230:114
12. Sijo AK, Jha VK, Kaykan LS, Dutta DP (2020) J Magnetism Magnetic Mater 497:166047
13. Poudel TP, Rai BK, Yoon S, Guragain D, Neupane D, Mishra SR (2019) J Alloy Compd 802:609
14. Gajula GR, Buddiga LR (2020) J Magnetism Magnetic Mater 494:165822
15. Ostafiychuk BK, Kaykan LS, Kaykan JS, Ya B, Deputat, Shevchuk OV (2017) Nanoscale Res Lett 12
16. Kaykan LS, Kaykan JS, Yaremiy IP, Ugorchuk OM, Deputat BY, Nykoliuk MO (2016) J Nano-Electron Phys 8:04066
17. Almessiere MA, Slimani Y, Rehman S, Khan FA, Polat EG, Sadaqat A, Shirsath SE, Baykal A (2020) Mater Sci Eng C 116:111186
18. Agostini M, Matic A, Panero S, Croce F, Gunnella R, Reale P, Brutti S (2017) Electrochim Acta 235:262
19. Hagh NM, Amatucci GG (2010) J Power Sources 195:5005
20. Kotsyubynsky VO, Grubiak AB, Moklyak VV, Pylypiv VM, Lisovsky RP (2016) Metallofiz Noveishie Tekhnol 36:1497
21. Arshad MI, Arshad S, Mahmood K, Ali A, Amin N, Umaid-ur-Rehman, Isa M, Akram A, Sabir N, Ajaz-un-Nabi M (2020) Physica B Condensed Matter 599:412496
22. Yokozaki R, Kobayashi H, Honma I Ceramics Int (2020)
23. Zhang Z (2020) Mater Today Commun 101734
24. Jha VK, Alam SN, Roy M (2019) J Supercond Nov Magn 33:455

25. Kaykan LS, Mazurenko JS, Sijo AK, Makovysyn VI (2020) Appl Nanosci 10:2739
26. El-Fadl AA, Abd-Elrahman MI, Younis N, Afify N, Abu-Sehly AA, Hafiz MM (2019) J Alloy Compd 795:114
27. Ferchmin AR, Klama S, Krompiewski S (1979) Czech J Phys 29:883
28. Gul S, Yousuf MA, Anwar A, Warsi MF, Agboola PO, Shakir I, Shahid M (2020) Ceram Int 46:14195
29. Kumar L, Kumar P, Kar M (2013) J Mater Sci Mater Electron 24:2706
30. Zaki HM, AL-Heniti SH, Aljwiher MM (2020) Physica B Condensed Matter 597:412382
31. Poole CP Jr, Farach HA (1982) Z Physik B Condensed Matter 47:55
32. Mondal RA, Murty BS, Murthy VRK (2014) Curr Appl Phys 14:1727
33. Ostafiychuk BK, Gasyuk IM, Kaykan LS, Uhorchuk VV, Yakubovskiy PP, Tsap VA, Kaykan YuS (2016) Metallofiz Noveishie Tekhnol 36:89
34. Mazurenko J (2020) Phys Chem Solid St 21:453
35. Dutta DP, Roy M (2017) Ceramics Int 43:16915